NANO · MICRO small
www.small-journal.com

Substrate Morphology Directs (001) Sb_2Se_3 Thin Film Growth by Crystallographic Orientation Filtering

*Joao Otavio Mendes, Andrea Merenda, Karen Wilson, Adam Fraser Lee, Enrico Della Gaspera, and Joel van Embden**

Antimony chalcogenide, Sb_2X_3 (X = S, Se), applications greatly benefit from efficient charge transport along covalently bonded (001) oriented $(Sb_4X_6)_n$ ribbons, making thin film orientation control highly desirable – although particularly hard to achieve experimentally. Here, it is shown for the first time that substrate nanostructure plays a key role in driving the growth of (001) oriented antimony chalcogenide thin films. Vapor Transport Deposition of Sb_2Se_3 thin films is conducted on ZnO substrates whose morphology is tuned between highly nanostructured and flat. The extent of Sb_2Se_3 (001) orientation is directly correlated to the degree of substrate nanostructure. These data showcase that nanostructuring a substrate is an effective tool to control the orientation and morphology of Sb_2Se_3 films. The optimized samples demonstrate high (001) crystallographic orientation. A growth mechanism for these films is proposed, wherein the substrate physically restricts the development of undesirable crystallographic orientations. It is shown that the surface chemistry of the nanostructured substrates can be altered and still drive the growth of (001) Sb_2Se_3 thin films – not limiting this phenomenon to a particular substrate type. Insights from this work are expected to guide the rational design of Sb_2X_3 thin film devices and other low-dimensional crystal-structured materials wherein performance is intrinsically linked to morphology and orientation.

1. Introduction

Chalcogenides with low-dimensional crystal structures, composed of quasi-2D layers or quasi-1D ribbons have been extensively explored for device applications.[1] Recently, special attention has been given to quasi-1D antimony chalcogenide phases (Sb_2S_3, Sb_2Se_3, and $Sb_2S_xSe_{3-x}$) with high efficiencies being achieved in a diverse range of applications, including photovoltaics,[2] water splitting,[3] energy storage,[4] and flexible photodetectors.[5] In contrast to typical quasi-2D and 3D materials (i.e., silicon, CdTe, and organo-metal perovskites),[1a] quasi-1D antimony chalcogenide crystals have naturally passivated grain boundaries and no dangling bonds.[6] Sb_2Se_3 has particularly attractive optical and electronic properties, including p- or n-type conductivity,[7] good electron and hole mobility (≈15 and ≈40 $cm^2\ V^{-1}\ s^{-1}$ respectively),[1a] and a high optical absorption coefficient (>10^5 cm^{-1}) through a 1.2 eV direct band gap.[8] Moreover, facile processing of thin films by thermal evaporation can be achieved owing to the low vapor pressure of Sb_2Se_3 and absence of crystal polymorphism.[9]

Antimony selenide crystallizes with an orthorhombic lattice in the space group #62. In the crystal structure, Sb atoms are bound by strong covalent bonds to Se atoms forming $(Sb_4Se_6)_n$ quasi-1D ribbons that extend along the [001] direction, while in the [100] and [010] directions ribbons interact only by weak van der Waals forces.[10] This ribbon assembly makes the electronic properties of Sb_2Se_3 crystals highly anisotropic.[11] This has given rise to the need to orient the crystal structure of Sb_2Se_3 films relative to the substrate to obtain high-performing thin film devices.

Crystallographic orientation control (texturing) to achieve the optimal alignment of the quasi-1D $(Sb_4Se_6)_n$ ribbons has been the focus of numerous research endeavors and has been proven to be intrinsically linked to the performance of Sb_2Se_3 devices.[12] For reference, **Figure 1**a shows the Sb_2Se_3 unit cell and ribbon structure, and the corresponding crystallographic directions. Poor charge transport is observed in directions orthogonal to the c-axis ([*hk*0] directions) due to the weak atomic interactions between ribbons. In entirely (*hk*0) oriented thin films, $(Sb_4Se_6)_n$ ribbons lie parallel to the substrate surface and therefore result in compromised electronic properties within vertical (sandwich) devices. Extensive research has shown that minimizing (*hk*0) orientations is beneficial to the efficiency of solar and photoelectrochemical cells.[13] Conversely, charge transport is far more efficient along the covalently bonded c-axis of the ribbon structure.

J. Otavio Mendes, A. Merenda, K. Wilson, A. Fraser Lee, E. Della Gaspera, J. van Embden
School of Science
RMIT University
Victoria 3001, Australia
E-mail: joel.vanembden@rmit.edu.au

The ORCID identification number(s) for the author(s) of this article can be found under https://doi.org/10.1002/smll.202302721

DOI: 10.1002/smll.202302721

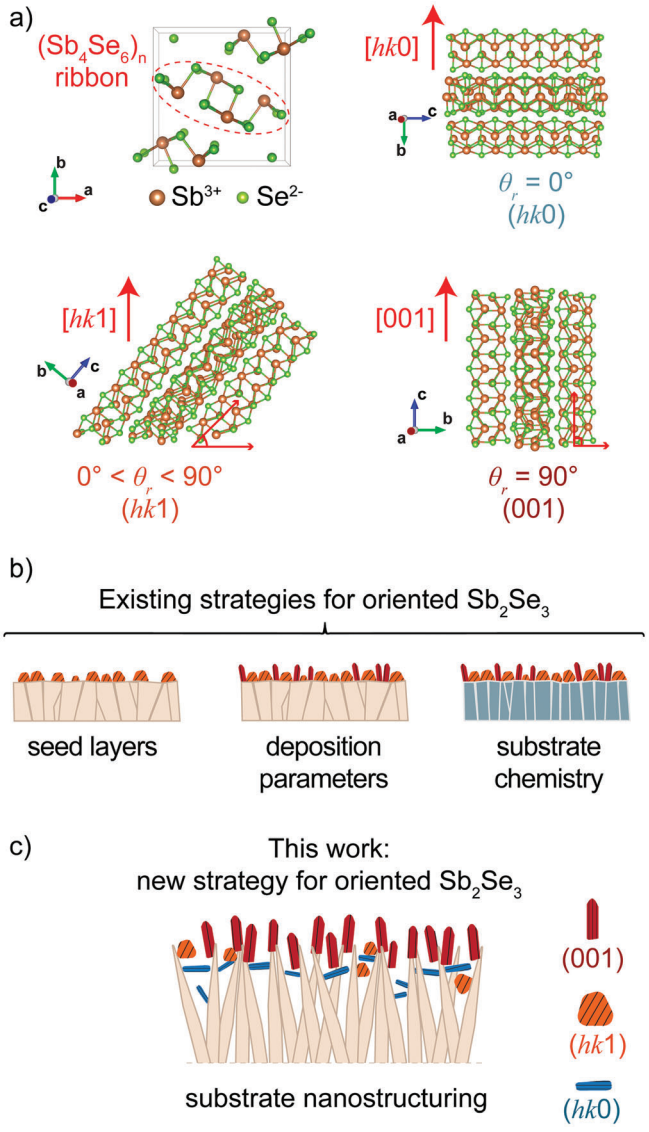

Figure 1. a) Schematic of an Sb_2Se_3 unit cell and the three possible "types" of ribbon orientation and their corresponding crystallographic notations. b) Schematic of existing strategies to achieve vertical ribbon orientation in Sb_2Se_3 thin films. c) Proposed methodology in this work, wherein surface nanostructure is used to direct crystal growth and (001) orientation.

As such, thin films with higher proportions of vertical ribbon orientation have improved charge transport properties, with the most optimal transport (between electrodes) being observed for (001) oriented thin films.[11a] Specifically, the diffusion length has been determined to be 1.7 µm in the [001] direction compared to only 0.29 µm in the [221] direction.[11b] We note here that several studies have settled for suboptimal textured Sb_2Se_3 films (usually with slightly preferential orientation along the [221] or [211] crystallographic directions) as these tend to present a compact morphology that is convenient for planar device applications.[14] However, a perfect (001) alignment is the most desirable to fully exploit facile charge transport along the ribbons. Thin films with a substantial degree of (001) orientation have achieved record performances in Sb_2Se_3 solar cells,[15] photoelectrochemical cells for water splitting,[16] photodetectors[17] and insertion battery electrodes.[18]

Although strategies to control the growth and orientation are key to designing efficient Sb_2Se_3 devices, orientation control of Sb_2Se_3 thin films is experimentally challenging. The thermodynamic tendency of crystal faces to grow with low energy (*hk*0) planes, i.e., (100), (010), (110), and (120),[13b] parallel to the substrate complicates orientation control. Current strategies to preferentially orient Sb_2Se_3 films involve extensive optimization of deposition parameters, which must be performed for each different substrate type. It is well established that the substrate material,[19] and their exposed crystal facets[20] are able to influence Sb_2Se_3 film orientation and morphology. Re-evaporation of undesired Sb_2Se_3 orientations to form oriented seed layers[21] and harnessing "nanoepitaxy"[22] have also been used to help direct crystal orientation. Figure 1b categorizes the extensive body of research on Sb_2Se_3 into three key types of approaches currently employed to orient Sb_2Se_3 thin films, including the use of a seed layer, optimizing deposition parameters, and tailoring substrate chemistry.[23]

The morphology (nanostructure) of the substrate is another important parameter that may influence Sb_2Se_3 grain growth and orientation. However, to date, the effect of substrate nanostructure on the morphology and orientation of evaporated Sb_2Se_3 films has remained unexplored. Controlled manipulation of substrate nanostructure (Figure 1c) constitutes an alternative approach to tune Sb_2Se_3 orientation. Harnessing this strategy allows the possibility to select the most desired substrate material (for electronic matching) and then use substrate nanostructure to direct the desired growth orientation and bulk morphology.

Here, the effect of substrate nanostructure on the growth of evaporated Sb_2Se_3 films is investigated for the first time. To accomplish this, Sb_2Se_3 thin films were grown on substrates possessing distinctly different physical surface structures. X-ray diffraction (XRD) and scanning electron microscopy (SEM) reveal the crucial role played by substrate nanostructure on final Sb_2Se_3 film orientation and morphology. A novel strategy to overcome fundamental challenges in the fabrication of (001) oriented Sb_2Se_3 thin films is presented.

2. Results and Discussion

2.1. Experimental Design and Understanding Ribbon Orientation

To study how substrate nanostructure affects film growth, we must first develop a clear understanding of crystal orientation in Sb_2Se_3 thin films. Here we use the *Pbnm* setting for the indexing of planes and crystallographic directions.[24] As outlined previously, charge transport is most efficient along the covalent length of the ribbon structure, and thus the physical phenomenon to be controlled is the ribbon orientation itself. When investigating the orientation (texture) of Sb_2Se_3 thin films, appropriate analysis requires that the orientation of a given crystal plane is associated to its ribbon orientation.[25] To achieve this, we define a ribbon tilt angle (θ_r) in relation to the substrate, and then group preferential crystallographic orientations in relation to ribbon tilt. All (*hk*0) orientations are those with ribbons that are parallel to the

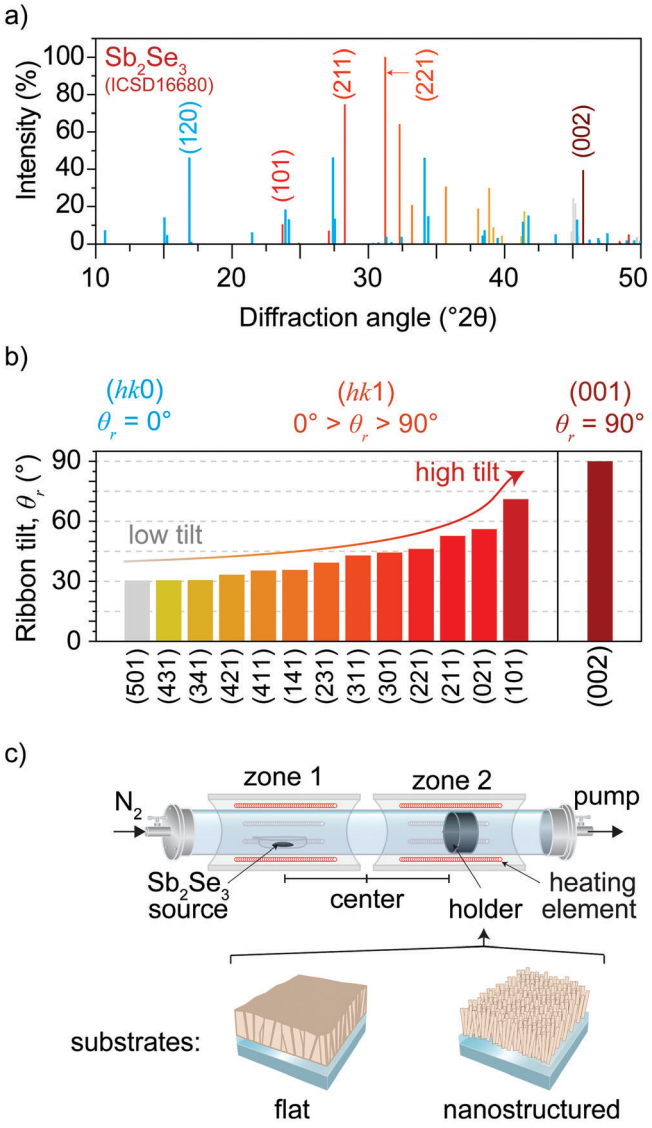

Figure 2. a) Theoretical XRD pattern of Sb_2Se_3 (ICSD#16680) color coded by ribbon orientation group (horizontal (*hk*0), blue; tilted (*hk*1), orange/red; vertical (001), brown). b) Relationship between Sb_2Se_3 crystal planes analyzed in this paper and $(Sb_4Se_6)_n$ ribbon tilt angle. c) Schematic of the VTD apparatus and the "flat" and "nanostructured" substrates employed in this work.

substrate and have $\theta_r = 0°$. Randomly orientated (*hkl*) Sb_2Se_3 thin films include ribbons with a range of orientations with $0° < \theta_r < 90°$. Finally, (*00l*) orientations are those with ribbons that extend vertically from the substrate, $\theta_r = 90°$. **Figure 2**a shows the calculated intensities of all reflections for Sb_2Se_3 between 10–50°2θ. For clarity, these have been divided into the three groups defined above. Specifically, (*hk0*) in blue, (*hkl*) in orange/red, and (00*l*) in brown.

For this work, we considered *all peaks* in the experimental XRD pattern between 10–50° 2θ that do not overlap with substrate peaks and have signal-to-noise ratios that allow their fitting. These comprised 25 reflections (11 (*hk*0), 13 (*hkl*), and the (002)), which are sufficient to accurately assess the crystallographic orientation of Sb_2Se_3 thin films and associated ribbons. We note here that (by coincidence) after discounting the (*hk*0) and (002) planes, the remaining (13) reflections of Sb_2Se_3 are all (*hk*1), i.e., (101), (211), (221), etc. Figure 2b shows all crystal planes relevant to Sb_2Se_3 thin film orientation as a function of ribbon tilt angle, specifically highlighting that (*hk*1) reflections span a range of ribbon tilt angles between 30–90°. Considering this, when specific reference is made to "(*hk*1) orientated" thin films in this work it must be remembered that these planes are spread across a large range of ribbon tilts, i.e., that (*hk*1) orientated thin films are not necessarily synonymous with favorably orientated (high ribbon tilt angle) films, as is sometimes implied in the literature.

Having examined the relationship between Sb_2Se_3 crystal and ribbon orientation, we now discuss our experimental methodology. Figure 2c illustrates the vapor transport deposition (VTD) reactor used in this work. Physical evaporation is the most common method employed for preparing Sb_2Se_3 thin films for device applications.[23h,26] VTD comprises an evaporation source with the desired amount of Sb_2Se_3 powder (source) located in zone 1. The substrate is placed in a graphite holder within zone 2 (set to a lower temperature). This configuration allows precise control of film thickness simply by varying the amount of Sb_2Se_3 in the source (see Experimental for further details). Prior to these studies, our VTD reactor was first optimized to achieve the controlled and reproducible growth of Sb_2Se_3 thin films.[13d]

Well-defined substrates are required to effectively investigate how substrate nanostructure controls the crystal growth and orientation of Sb_2Se_3 thin films. ZnO was selected as the substrate, and fabricated with two distinct morphologies: nanostructured films (ZnO-NW); and compact flat films (ZnO-Flat). ZnO is an ideal substrate as both flat and nanostructured thin films can be produced with the same orientation (same ZnO crystal planes at the surface) using chemical bath deposition (CBD), enabling investigation into the impact of substrate morphology alone on Sb_2Se_3 film texture. Details on the fabrication and characterization of ZnO substrates are provided in the Experimental and Supporting Information (Figure S1, Supporting Information).

2.2. Growth of Sb_2Se_3 Films on Nanostructured and Flat Substrates

Sb_2Se_3 film growth on ZnO-Flat and ZnO-NW substrates was investigated by SEM and XRD as a function of Sb_2Se_3 film thickness. Isolating samples with different thicknesses (beginning from ultra-thin films) provides snapshots of thin film growth dynamics. Notably, except for varying the mass of Sb_2Se_3 powder in the evaporation source, layers corresponding to the different stages of film growth were obtained under identical VTD conditions. **Figure 3** shows cross-sectional SEM images as a function of Sb_2Se_3 source mass, and the corresponding texture coefficients of 25 key crystallographic planes grouped into (*hk*0), (*hk*1), and (001) orientations as previously defined. XRD patterns for each Sb_2Se_3 film are presented in Figure S2 (Supporting Information).

Remarkably, these data reveal that Sb_2Se_3 film morphology and crystallographic orientation vary drastically between Sb_2Se_3 layers grown on flat and nanostructured substrates. Under

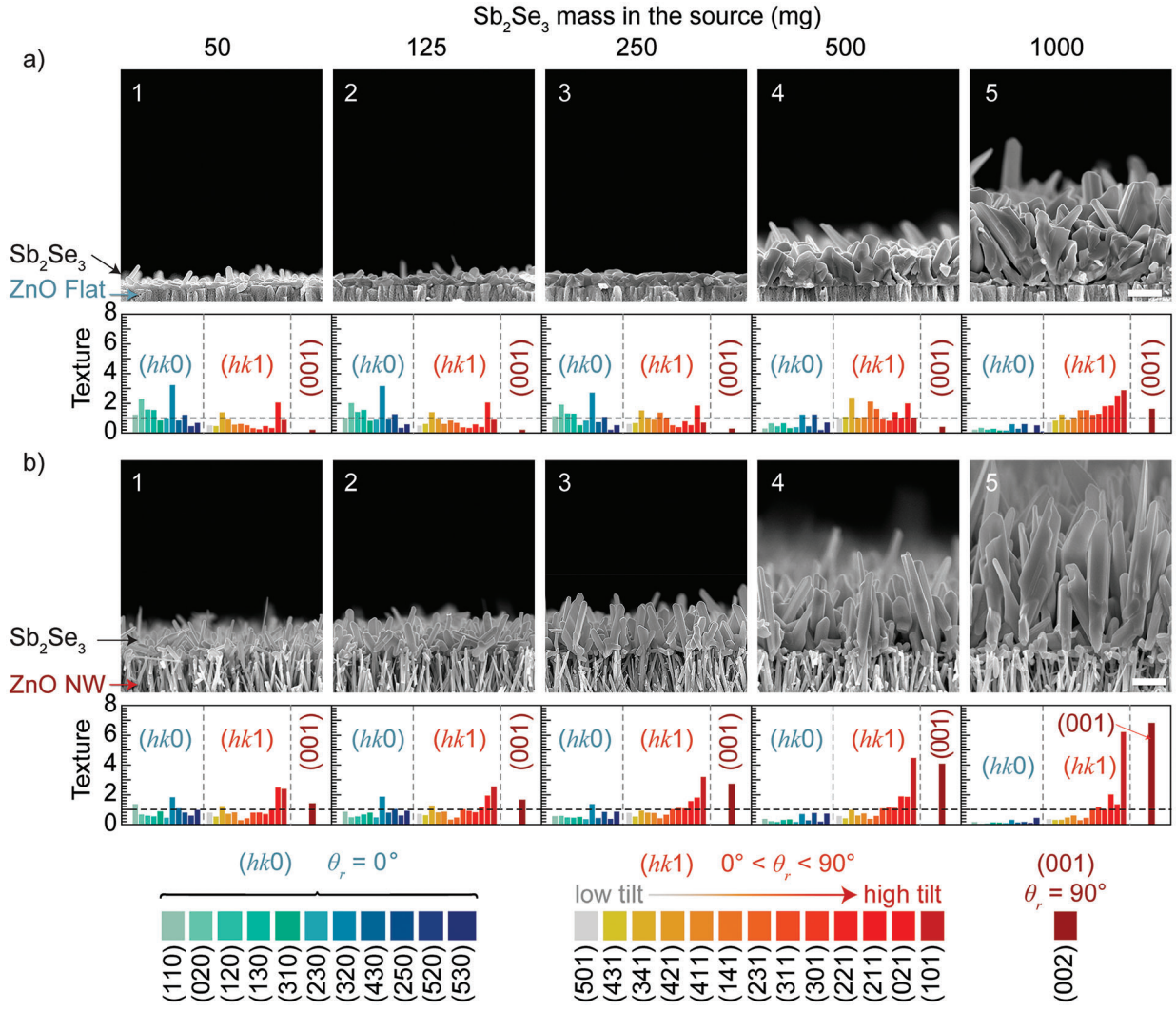

Figure 3. SEM images and corresponding texture coefficients color coded by ribbon tilt angle for Sb_2Se_3 thin films as a function of Sb_2Se_3 source mass (film thickness). a) Sb_2Se_3 deposited ZnO-Flat substrates and b) Sb_2Se_3 deposited ZnO-NW substrates. Scale bars are 500 nm.

otherwise identical VTD conditions (source evaporation rates), flat substrates result in the deposition of a compact relatively unoriented films, while the nanostructured substrate drives the growth of highly (001) oriented Sb_2Se_3 films. Figure 3a (panels 1 to 3) reveal a compact Sb_2Se_3 layer nucleating on the surface of the ZnO-Flat substrate. From the corresponding crystallographic textures, Sb_2Se_3 films initially grow with (*hk*0) preferential orientation (panel 1), evidenced by the vast majority of (*hk*0) texture coefficients (TC) above TC = 1, and the low (*hk*1) textures that are mostly well below TC = 1. Notably, for the thinnest films (in the early stages of film growth) vertical (001) crystal growth is strongly disfavored by the flat substrate ($TC_{(002)}$ = 0.23). As the film thickness increases, they form moderately (*hk*1) oriented films, with a slight preference for those orientations at higher ribbon tilt angles.

Growth governed by the evolution selection principle is invoked to explain the change in preferential texture observed for Sb_2Se_3 films grown on ZnO-Flat substrates. This principle states that during film deposition preferential texture evolves when crystals with faster vertical growth rates overgrow and progressively bury (suppress) crystals with slower growth rates.[27] In Sb_2Se_3 films, crystals oriented in a way that expose (*hk*1) crystallographic planes will have higher vertical growth rates than (*hk*0) oriented crystals.[13b,21,22] Hence, as the Sb_2Se_3 films grow (on flat substrates) the relative population density of (*hk*1) oriented crystals will naturally tend to increase. This growth mechanism is illustrated in Figure S3 (Supporting Information). As observed here, the Sb_2Se_3 thin film starts growing slightly (*hk*0) oriented, with only a few (*hk*1) oriented grains. However, those crystals with (*hk*1) planes exposed at the surface eventually overgrow the other crystals due to their higher growth rates. A shift in preferential orientation occurs (Figure 3a, panel 3–4) when the population density of crystals at the surface becomes dominated by overgrown (*hk*1) grains, eventually giving rise to the slight (*hk*1) orientation observed in mature thin films (Figure 3a, panel 5).

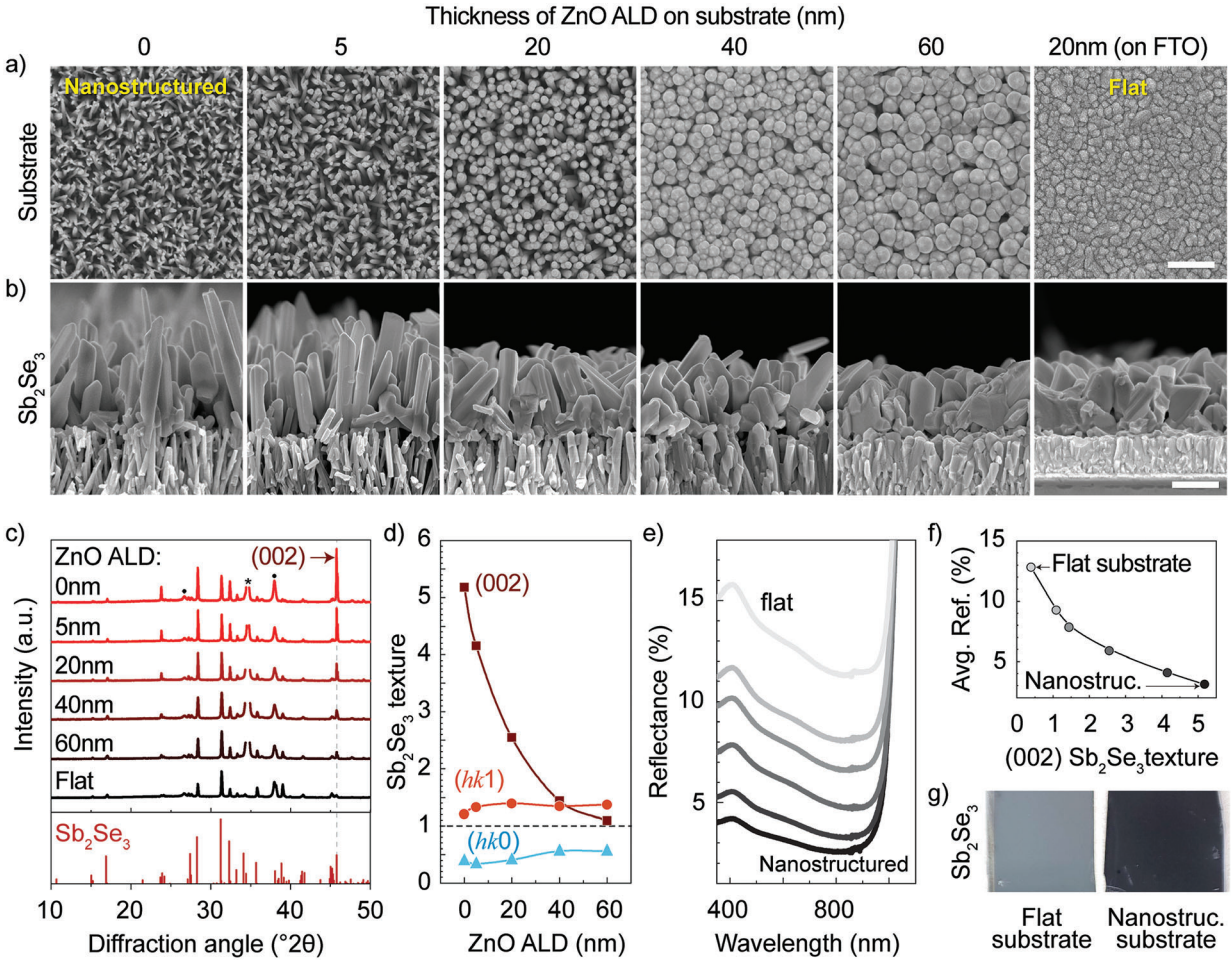

Figure 4. a) Top view SEM images of ZnO-NW substrates coated with 0, 5, 20, 40, and 60 nm ZnO via ALD (and ZnO ALD on FTO), respectively. b) Cross-section SEM images of Sb_2Se_3 films obtained on the substrates shown in the upper panels. c) XRD patterns of Sb_2Se_3 films as a function of ZnO ALD coating. d) Texture coefficient as a function of ZnO ALD coating thickness. e) Reflectance measurement of corresponding samples, wherein lighter colors indicate Sb_2Se_3 films deposited on flatter substrates. f) Average reflectance (400–900 nm) as a function of Sb_2Se_3 (002) texture. g) Photographs of Sb_2Se_3 films on flat and nanostructured substrates, highlighting light-trapping by the oriented Sb_2Se_3 NR film. Scale bars correspond to 500 nm.

In stark contrast, Figure 3b shows that under the same VTD conditions, the ZnO-NW substrate drives the formation of vertically oriented Sb_2Se_3 ribbons. For the thicker films shown in Figure 3b (panels 4 and 5), exceptionally high textures are observed for (101) and (002) crystal planes (71° and 90° tilt, respectively), with low-tilt (*hk*1) and (*hk*0) orientations almost completely suppressed by the nanostructured substrate. The exceptional degree of (001) orientation observed here may be traced back to the early stages of film growth. The orientation of the thinnest films (Figure 3b, panels 1 and 2) already exhibits a slight (*hk*1) preference at high tilt angles. As the film evolves, only those textures from the highest ribbon tilt angles increase, culminating in highly (001) oriented nanorod (NR) array. Reports of Sb_2Se_3 NR arrays preferentially aligned in [221] or [211] directions are common in the literature.[15a,22] However, such films have a low proportion of vertical (001) oriented Sb_2Se_3 grains. The thicker films fabricated here (Figure 3b, panels 4 & 5) are comparable to the highest (001) oriented films previously reported.[17a,25,28]

2.3. Orientation Control of Sb_2Se_3 Films

To confirm a direct correlation between Sb_2Se_3 film orientation and substrate nanostructure, Sb_2Se_3 thin films were deposited on substrates whose surfaces were gradually modified from highly nanostructured to flat, by conformal coating of ZnO-NW substrates with ZnO via ALD. The number of ALD cycles was progressively increased until the space between wires in the ZnO-NW array was filled and a flat substrate obtained. **Figure 4**a presents top view SEM images of these substrates, beginning from untreated ZnO-NW ("nanostructured") and proceeding to ZnO-NW coated with 5, 20, 40, and 60 nm ZnO layers via ALD. A final control sample with an even smoother substrate was obtained by depositing 20 nm ZnO via ALD directly on FTO ("flat"). Sb_2Se_3 thin films were then deposited on these substrates in a single VTD deposition using the previously described parameters.

Analysis of the SEM images in Figure 4b evidence a change in Sb_2Se_3 film morphology from a vertically aligned Sb_2Se_3 NR array to a dense compact thin film as the substrate flattens. Corresponding XRD patterns (Figure 4c) highlight a concomitant gradual disappearance of the (002) reflection as the substrate becomes less nanostructured. Texture coefficient analysis of these XRD patterns is shown in Figure 4d. As established, Sb_2Se_3 films deposited on highly nanostructured substrates are substantially (001) oriented, display little preference for (*hk*1) growth, and have greatly suppressed (*hk*0) orientations. Importantly, the (002) texture coefficient is seen to steadily decrease to TC∼1, giving way to a higher proportion of randomly oriented ribbons as the substrate flattens and becomes more uniform. Full analysis correlating ribbon tilt to substrate structural parameters is provided in Figure S4 (Supporting Information), which highlights that even small changes in the thickness or density of ZnO NW leads to measurable variations in Sb_2Se_3 ribbon orientation. Collectively, these data indisputably confirm a direct link between substrate nanostructure and the growth of (001) oriented Sb_2Se_3 thin films. To our knowledge, this is the first example of bulk substrate nanostructure directing the oriented growth of Sb_2Se_3 thin films.

Considering the multitude of optoelectronic applications that exploit Sb_2Se_3 thin films, a noteworthy characteristic of our Sb_2Se_3 NR films is their ability to harvest incident light. It is well-known that highly nanostructured films possess light-trapping capacity, wherein light that penetrates the surface becomes trapped and is eventually absorbed.[29] Figure 4e shows reflectance measurements of Sb_2Se_3 films as a function of substrate nanostructure. A significant decrease in reflectance across the entire visible spectral range is observed with increasing (001) orientation. Figure 4f highlights an inverse correlation between the average reflectance (400–900 nm) and the degree of Sb_2Se_3 (002) texture. Highly (001) oriented Sb_2Se_3 NR thin films exhibit a remarkably low average reflectance of only 3.1%. This contrasts with (traditional) compact, randomly oriented Sb_2Se_3 thin films deposited on flat substrates, wherein the reflectance is more than 4x higher (12.8%). For reference, Sb_2Se_3 films deposited on flat CdS substrates have average film reflectance values as high as 33% (see Figures S5 and S6, Supporting Information). Extensive light-trapping by the Sb_2Se_3 NR array is readily observed from photographs of the as-prepared Sb_2Se_3 films (Figure 4g). Light trapping is highly desirable for solar cells and photodetectors, as well as photoelectrochemical and photocatalytic applications (such as water splitting); hence substrate nanostructure should be a key design consideration for Sb_2Se_3 light absorbers in such applications.

To highlight their optical activity, proof-of-concept Sb_2Se_3 NR photodetectors were fabricated (Figure S7, Supporting Information). Our NW photodetectors show a strong photoresponse to red light (625 nm) with a large ON/OFF ratio > 10^4 even at low illumination power (8 mW cm^{-2}), comparable with other devices in reported in the literature.[30] For comparison we also developed photodetectors with a ZnO-NW/CdS interface, which show improved photocurrents, highlighting the importance of interface chemistry on current collection. Given the large number of methods available in the current literature for making nanostructured substrates, it is expected that the photoactive and light trapping thin films developed here will have a broad range of applications.

2.4. Growth Mechanism of Sb_2Se_3 on Nanostructured Substrates

Having established that substrate nanostructure strongly influences the preferential orientation and morphology of Sb_2Se_3 grains (and $(Sb_4Se_6)_n$ ribbons), we now consider the underpinning growth mechanism. The evolution selection principle explains the general trends in Sb_2Se_3 thin film orientation on flat substrates, factoring in deposition conditions and the substrate surface, but cannot account for the highly (001) oriented thin films generated in this work. We therefore propose a film growth mechanism based on the physical selection of (001) oriented crystals, whereby (*hk*0) Sb_2Se_3 crystals are *filtered out* by the ZnO-NW array at the early stages of film growth. This mechanism is schematically represented in **Figure 5**a and consists of three main stages: i) nucleation (initial deposition); ii) confinement of (*hk*0) and low tilt (*hk*1) oriented crystals growing between nanowires; and iii) fast [001] crystal growth.

The ZnO-NW film surface has significant gaps between the nanowires. As such, in early stages of growth Sb_2Se_3 vapor will penetrate the NW array and nucleate on the sides of the ZnO NWs. From Figure 3b we recall that the early stages of Sb_2Se_3 film growth are characterized by an almost equal degree of (*hk*0) and (*hk*1) texture (TC∼1), wherein further growth resulted in a large increase in (*hk*1) textures only at high tilt angles and the suppression of (*hk*0) orientations. As such, the nanostructured substrate halts the growth of all (*hk*0) and low tilt (*hk*1) oriented crystals very early during film deposition, i.e., the ZnO-NW array must act as a physical barrier to filter out the maturation of low ribbon tilt Sb_2Se_3 crystals. This is evidenced by the back-scattered SEM image in Figure 5b (obtained from an Sb_2Se_3 film in the early stage of growth, viz. Figure 3b, Panel 1), which reveals horizontal (*hk*0) and low-tilt (*hk*1) Sb_2Se_3 crystals trapped within the ZnO-NW array, and the evolution of near-vertical (001) grains emerging from the NW surface. It follows that a NW array comprising wider (denser) wires results in a substrate with lower surface porosity that will be less effective in trapping crystals with low ribbon tilt, and hence less effective in directing [001] growth, consistent with the data of Figure 4d wherein (002) texture decreases with substrate infilling. Physical confinement of (*hk*0) and (*hk*1) oriented crystals during nascent Sb_2Se_3 film growth is followed by a standard growth regime, wherein (001) oriented crystals that have been selected by *orientation filtering* dominate the surface, rapidly consuming "Sb_2Se_3" vapor to yield highly (001) oriented thin films. Figure 5c shows the back-scattered SEM image of a thick (≈1 µm) Sb_2Se_3 film, showing highly (001) orientated crystals and small underdeveloped (*hk*0) and low tilt (*hk*1) crystals trapped in the ZnO-NW array.

HRTEM of a single Sb_2Se_3 NR physically extracted from a mature Sb_2Se_3 film deposited on nanostructured ZnO (Figure 5d) has an interplanar spacing of 0.582 nm (Figure 5e), matching the d-spacing between (200) planes of *Pbnm* Sb_2Se_3. These images confirm that the covalent $(Sb_4Se_6)_n$ 1D ribbons (illustrated in Figure 5f) are aligned to the longer (vertical) axis of the NR crystal. Figure 5g shows the selected area electron diffraction (SAED) of the nanorod from panel d. The relationship between (101) and (200) diffraction spots correspond to a [010] crystallographic axis – orthogonal to the (001). Importantly, the discrete nature of diffraction spots indicates the Sb_2Se_3 NR is a single crystal – a property highly beneficial to charge transport and associated

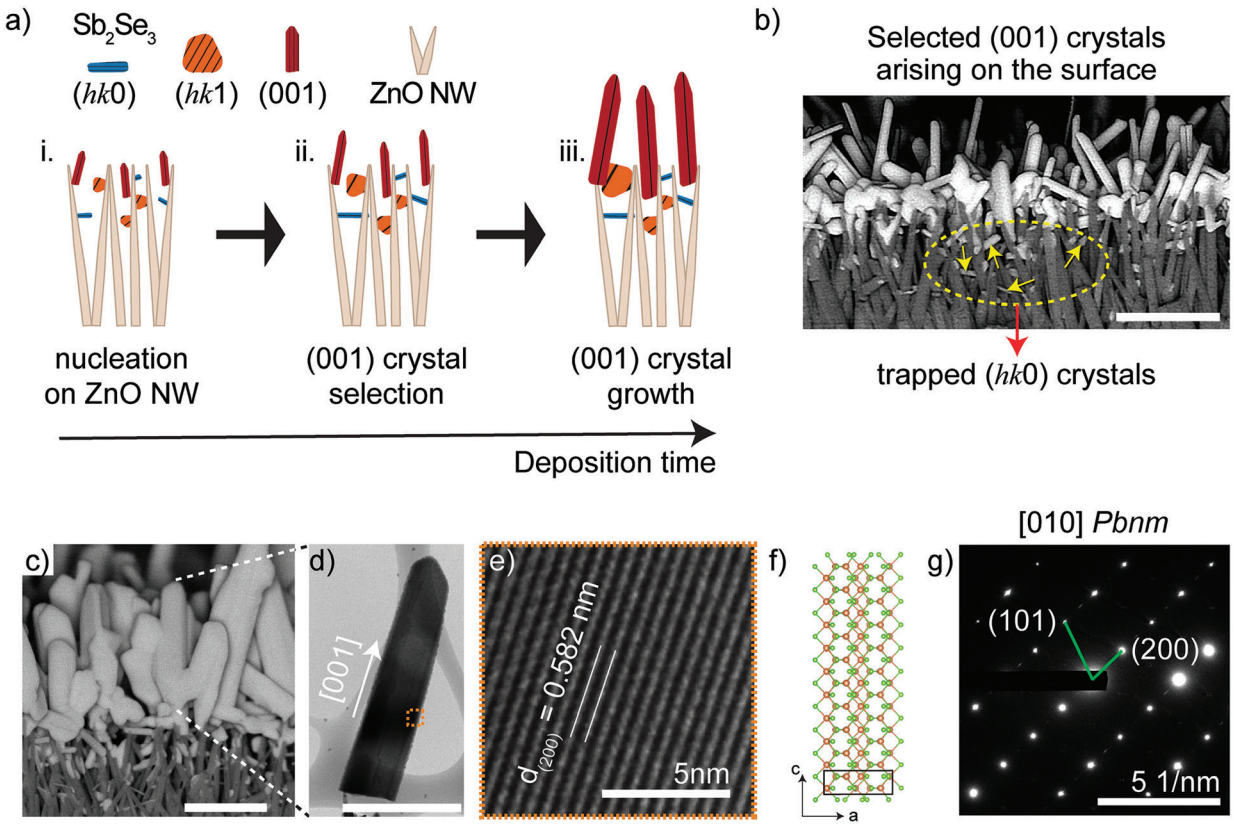

Figure 5. a) Proposed mechanism of Sb_2Se_3 crystal growth on ZnO-NW to form highly (001) oriented films. b) Backscattered SEM (BS-SEM) image of an Sb_2Se_3 thin film in the early stages of deposition, highlighting trapped Sb_2Se_3 crystals. c) BS-SEM image of a mature (thicker) Sb_2Se_3 film. d) TEM image of a single crystal physically extracted from (c). e) HRTEM of a single Sb_2Se_3 NR showing the lattice planes. f) Crystal structure of a single $(Sb_4Se_6)_n$ ribbon and Sb_2Se_3 unit cell. g) Selected-area electron diffraction (SAED) pattern of (d). Unless indicated, scale bars correspond to 500 nm.

applications. Collectively, SEM and HRTEM confirm the orientation filtering process (from the initial stages of film development) and verify that Sb_2Se_3 NR array is composed of (001) vertically aligned monocrystalline Sb_2Se_3 NRs.

2.5. Surface Chemistry of the Nanostructured Substrate

To explore the flexibility of our approach to orient Sb_2Se_3 thin films, different substrate surface chemistries were investigated. If orientation control is purely a consequence of physical confinement within a nanostructured substrate, then Sb_2Se_3 crystal growth should be largely independent of the substrate type and surface chemistry (provided the substrate morphology can trap nascent crystals with low ribbon tilt angles). To test this hypothesis, Sb_2Se_3 was grown on ZnO-NW substrates coated with Al_2O_3, TiO_2 and CdS, which exhibit diverse bond dissociation energies: Ti–O 662 kJ mol^{-1}; Al–O 512 kJ mol^{-1}; and Cd–S 196 kJ mol^{-1}; compared with Zn–O 284 kJ mol^{-1}.[31] Such coated substrates will exhibit different abilities to bond with Sb_2Se_3, and hence different orientation preferences.[21] The Al_2O_3, TiO_2 (and ZnO) conformal coatings were deposited via ALD (≈5 nm), and the CdS by SILAR (≈10 nm) (**Figure 6**a) to preserve the underlying ZnO-NW morphology. These experiments include a ZnO ALD coated ZnO-NW substrate as an internal standard as well as control samples with identical coatings deposited on flat FTO substrates (SEM and XPS characterization of substrates provided in Figure S8, Supporting Information).

XRD patterns of Sb_2Se_3 samples exhibited higher intensity (002) reflections for all nanostructured substrates regardless of their surface composition (Figure 6b). Corresponding texture coefficients (Figure 6c) confirm that the degree of (002) texture is significantly higher for Sb_2Se_3 films deposited on coated ZnO-NW (red bars) compared to their flat counterparts (blue bars), irrespective of the coating type. A complete analysis of texture coefficients for films deposited on the coated substrates is shown in Figure S9 (Supporting Information). The somewhat lower (002) textural preference in the case of CdS is attributed to the less uniform and thicker coating typical of SILAR deposition versus highly conformal ALD coatings. This observation is consistent with previously established data (from Figure 4), wherein any increase in the NW coating thickness reduces the gaps between wires, and therefore the selectivity towards (001) oriented thin films. As seen by comparing the SEM images in Figure 6d, despite significantly different surface chemistry (TiO_2, Al_2O_3, CdS) the nanostructured ZnO-NW substrate drives the growth of favorably oriented vertical Sb_2Se_3 NR arrays. Top-view SEM images further highlight the similar morphology of Sb_2Se_3 films deposited on TiO_2, Al_2O_3, and CdS coated ZnO-NW (Figure S10, Supporting Information). Importantly, we stress that TiO_2, Al_2O_3

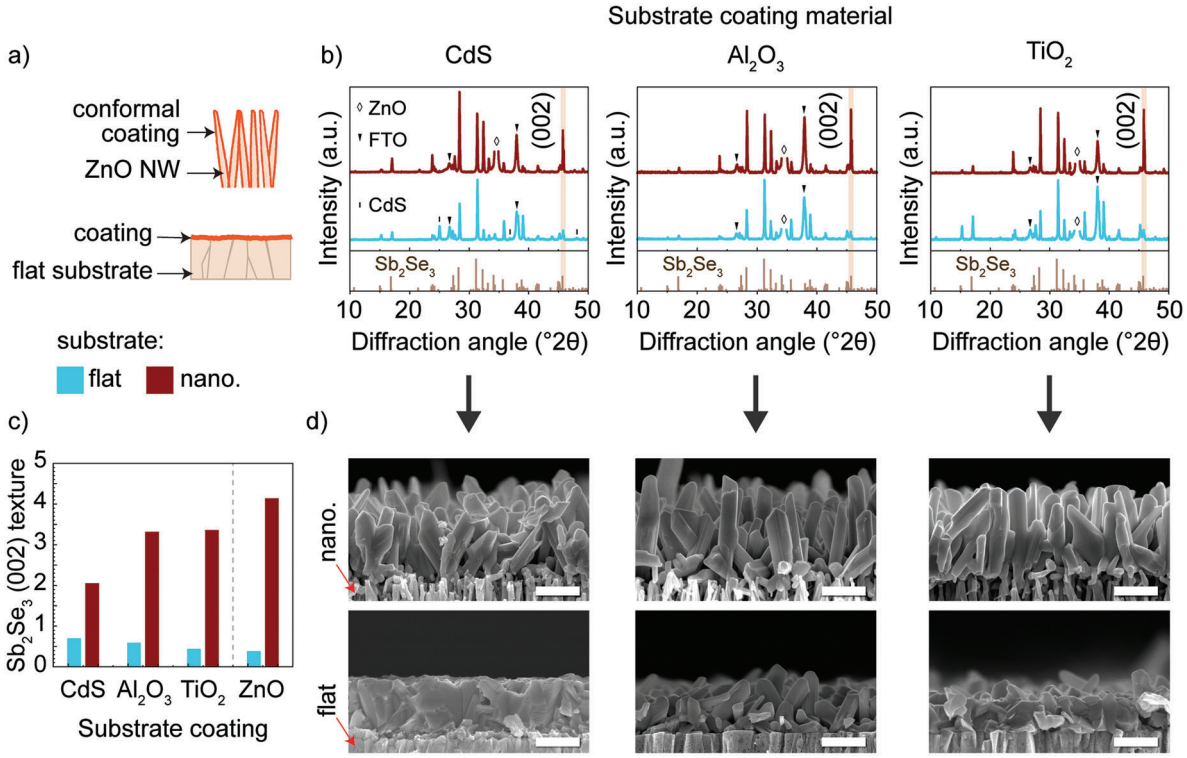

Figure 6. a) Schematic of coated nanostructured and flat substrates. b) XRD patterns of Sb_2Se_3 films with CdS, Al_2O_3, and TiO_2 coatings on flat FTO and ZnO-NW substrates, c) (002) textures calculated from the XRD patterns shown in (b), d) cross-sectional SEM images of Sb_2Se_3 films on the indicated substrates. Scale bars correspond to 500 nm.

and CdS coatings grown on flat substrates yield compact Sb_2Se_3 films in which the (001) orientation is suppressed ($TC_{(002)} << 1$). Collectively, these results confirm that *the structure of the underlying substrate dictates the deposition dynamics* and may be used as a tool to obtain highly (001) oriented Sb_2Se_3 films independent of surface chemistry. This discovery enables flexibility in the future design of functional nanostructured substrates and opens the door to unexplored substrate-film combinations for device application.

3. Conclusions

A new method to obtain preferentially oriented Sb_2Se_3 thin films via physical confinement effects (*orientation filtering*) is demonstrated. The morphology and orientation of Sb_2Se_3 films were investigated as a function of substrate nanostructure for films deposited via VTD. Exceptionally highly (001) oriented Sb_2Se_3 films were obtained on highly nanostructured substrates, while more compact and randomly oriented films were obtained on flat substrates. Fine control over Sb_2Se_3 film morphology and orientation is achievable by gradually manipulating the substrate nanostructure. A mechanism based on the preferential trapping (filtering out) of (*hk*0) and low tilt (*hk*1) crystals within a substrate nanowire array accounts for the high degree of (001) orientation obtained for Sb_2Se_3 films. As this mechanism is physical, we expect it will translate to other 1D crystal structure materials (including other antimony chalcogenides). Finally, we showed that the surface chemistry of our nanostructured substrates can be altered and still drive the growth of highly (001) oriented Sb_2Se_3 thin films – not limiting this phenomenon to a particular substrate type. Consequently, the thin films developed herein should be directly implementable within a range of Sb_2Se_3 devices that require specific surface chemistries. Likewise, with additional efforts on substrate design (geometry) and composition, the methodology outlined here provides an avenue to new device architectures based on template-driven crystallographic orientation. This work constitutes an important advance in the development of antimony chalcogenide-based applications, such as solar cells, photocatalytic devices, sensors, and batteries, wherein performance is intrinsically linked to morphology and orientation.

4. Experimental Section

Materials: Antimony(III) Selenide (99.999%) 200 mesh was purchased from China Rare Metal. Ethanolamine (99%), zinc acetate dihydrate (99%), 2-methoxyethanol (99.9%), $Zn(NO_3)_2$ (≥99.0%), ammonium citrate dibasic (98%), sodium sulfide nonahydrate (≥99.99%), Diethyl zinc (DEZ) (>52 wt.% Zn), trimethylaluminium (TMA) (97%), and titanium tetrachloride (TTC) (99.995%) were acquired from Sigma Aldrich. Ammonia solution (25 vol%) was purchased from ChemSupply Australia. FTO-coated glass was bought from Latech Scientific Supply (15 Ω sq^{-1}). Diethyl zinc (DEZ) (>52 wt.% Zn) was purchased from Sigma Aldrich. All reagents and solvents were used as received without further purification.

ZnO-NW and ZnO-Flat Substrates: Nanostructured and flat ZnO were deposited via chemical bath deposition (CBD) on glass/FTO (ZnO seeded) substrates.[32] First, substrates were cleaned in soapy water, acetone and IPA ultrasonic baths for 10 min in each solution. ZnO seeds were

then deposited via a sol–gel method. Specifically, the sol–gel solution was prepared by adding ethanolamine (105 µL) to 0.35 M zinc acetate dihydrate in 2-methoxyethanol (5 mL). The mixture was left to stir for ≈2 h until a completely clear solution was obtained followed by filtering through a 0.22 µm PTFE syringe filter. This sol–gel solution was spun on clean glass/FTO substrates at 4000 rpm for 30 s. Two layers were deposited to ensure full coverage (≈30 nm, as measured by profilometry). Substrates were heated at 200 °C for ≈2 min between layers, before final annealing at 250°C for 60 min in air. To deposit ZnO-NW, the seeded substrates were inclined inside a small (≈25 mL) beaker with the reactive (seeded) surface facing downwards. Aqueous $Zn(NO_3)_2$ (20 mM in ≈0.8 vol% NH_3) was then added to cover the substrate. The beaker was then placed in a water bath at 80 °C for exactly 60 min. Deposition was stopped by transferring substrates to a Milli-q water bath. Films were dried under a N_2 gas stream. To achieve "ZnO-Flat" samples, ammonium citrate (2 mM) was added to the initial growth solution. All ZnO-NW and ZnO-Flat substrates were annealed at 500 °C for ≈1 h before being used.

ZnO-NW Coatings: ZnO, TiO_2, and Al_2O_3 were deposited via atomic layer deposition (ALD). The number of ALD cycles was calibrated (using ellipsometry) to yield the desired layer thickness. CdS was deposited via Successive Ionic Layer Adsorption and Reaction (SILAR).[33] See Supporting Information for details of these synthetic procedures.

Sb_2Se_3 Deposition: An optimized vapor transport deposition (VTD) method was used to deposit the Sb_2Se_3 films, as previous described.[13d] In short, the Sb_2Se_3 source (quartz crucible with Sb_2Se_3 powder) was put at the center of the left heating zone of a dual-zone furnace (equipped with a quartz tube). The mass of Sb_2Se_3 powder in the crucible was varied from 50 to 1000 mg according to the desired film thickness. Substrates were mounted within the right heating zone on a near vertical graphite holder positioned 10 cm from the furnace center. Pressure was equilibrated at 0.5–0.7 Pa before starting the heating program. Both zones were then heated at 250 °C for 30 min. The left zone, containing the Sb_2Se_3 source, was then heated to 540 °C over the course of 15 min (≈20 °C min^{-1}) and the temperature was held at 540 °C for 10 min. The right zone, containing the substrates, was kept at 250 °C through the whole process. The furnace was left to cool naturally for ≈2 h before ambient pressure was restored by bleeding N_2 gas into the tube.

Instrumentation: The scanning electron microscope (SEM) images and backscattered SEM (BS-SEM) images were taken on a FEI Verios 460L XHR-SEM equipped with in-lens secondary electron detector (TDL) and in-column backscattered detector (ICD). Transmission electron microscope (TEM, HR-TEM) images and selected area electron diffraction (SAED) patterns were taken on a JEOL JEM-2100 FEGTEM at 200 kV. X-ray diffraction (XRD) patterns were obtained using a Bruker AXS D4 Endeavour diffractometer with a Cu-K_α radiation source. Reflectance spectra were collected on a Cary 7000 UV–vis–NIR spectrophotometer equipped with an integrating sphere. X-ray photoelectron spectra (XPS) were collected on a Thermo Scientific K–alpha XPS instrument equipped with monochromated Aluminum K_α source (1486.7 eV). Atomic Force Microscope (AFM) images were obtained on an Asylum Research MFP-3D Infinity AFM. ALD was conducted on a commercial Arradiance GEMStar benchtop XT-S thermal ALD reactor. Ex-situ ellipsometric measurements were conducted on a M-2000 Spectroscopic ellipsometer (J.A. Woollam). The analysis was carried out at a fixed incident angle of 65° over a spectral range of 250–1500 nm. Curve fitting and thickness modeling were conducted on Complete EASE software, employing a Cauchy model to study the metal oxide layers.

Supporting Information

Supporting Information is available from the Wiley Online Library or from the author.

Acknowledgements

The Australian Research Council is acknowledged for supporting this work through grants DE150100427, DE170100164, DP190101864, DP200100313, and LE210100100. The authors acknowledge the facilities and the technical assistance of the RMIT University's Microscopy and Microanalysis Facility (RMMF) and MicroNano Research Facility (MNRF).

Open access publishing facilitated by RMIT University, as part of the Wiley - RMIT University agreement via the Council of Australian University Librarians.

Conflict of Interest

The authors declare no conflict of interest.

Data Availability Statement

The data that support the findings of this study are available from the corresponding author upon reasonable request.

Keywords

alignment, antimony selenide, epitaxy, nanostructures, solar, vapor transport deposition

Received: March 31, 2023
Revised: May 1, 2023
Published online:

[1] a) S. Hadke, M. Huang, C. Chen, Y. F. Tay, S. Chen, J. Tang, L. Wong, *Chem. Rev.* **2022**, *122*, 10170; b) W. Yang, X. Zhang, S. D. Tilley, *Chem. Mater.* **2021**, *33*, 3467; c) Y. Wang, Y. Zhao, X. Ding, L. Qiao, *J Energy Chem* **2021**, *60*, 451; d) R. Kondrotas, C. Chen, X. Liu, B. Yang, J. Tang, *J. Semicond.* **2021**, *42*, 031701; e) J. He, Y. Wei, T. Zhai, H. Li, *Mater. Chem. Front.* **2018**, *2*, 437.

[2] a) S. Barthwal, R. Kumar, S. Pathak, *ACS Appl Energy Mater* **2022**, *5*, 6545; b) U. A. Shah, S. Chen, G. M. G. Khalaf, Z. Jin, H. Song, *Adv. Funct. Mater.* **2021**, *31*, 2100265; c) A. Mavlonov, T. Razykov, F. Raziq, J. Gan, J. Chantana, Y. Kawano, T. Nishimura, H. Wei, A. Zakutayev, T. Minemoto, X. Zu, S. Li, L. Qiao, *Sol. Energy* **2020**, *201*, 227; d) R. Kondrotas, C. Chen, J. Tang, *Joule* **2018**, *2*, 857; e) X. Wang, R. Tang, C. Wu, C. Zhu, T. Chen, *J Energy Chem* **2018**, *27*, 713; f) Y. Zhao, S. Wang, C. Li, B. Che, X. Chen, H. Chen, R. Tang, X. Wang, G. Chen, T. Wang, J. Gong, T. Chen, X. Xiao, J. Li, *Energy Environ. Sci.* **2022**, *15*, 5118.

[3] a) S. Chen, T. Liu, Z. Zheng, M. Ishaq, G. Liang, P. Fan, T. Chen, J. Tang, *J Energy Chem* **2022**, *67*, 508; b) W. Yang, J. Moon, *J. Mater. Chem. A* **2019**, *7*, 20467; c) W. Yang, J. H. Kim, O. S. Hutter, L. J. Phillips, J. Tan, J. Park, H. Lee, J. D. Major, J. S. Lee, J. Moon, *Nat. Commun.* **2020**, *11*, 861; d) R. R. Prabhakar, T. Moehl, S. Siol, J. Suh, S. D. Tilley, *Chem. Mater.* **2020**, *32*, 7247.

[4] a) L. Xia, Z. Yang, B. Tang, F. Li, J. Wei, Z. Zhou, *Small* **2021**, *17*, 2006016; b) R. Gusmão, Z. Sofer, J. Luxa, M. Pumera, *ACS Sustainable Chem. Eng.* **2019**, *7*, 15790; c) S. Dong, C. Li, X. Ge, Z. Li, X. Miao, L. Yin, *ACS Nano* **2017**, *11*, 6474; d) S. Wang, X. Yang, P.-K. Lee, A. L. Rogach, D. Y. W. Yu, *Chem. Mater.* **2019**, *31*, 2469; e) P. V. Prikhodchenko, J. Gun, S. Sladkevich, A. A. Mikhaylov, O. Lev, Y. Y. Tay, S. K. Batabyal, D. Y. W. Yu, *Chem. Mater.* **2012**, *24*, 4750.

[5] a) X. Wen, Z. Lu, L. Valdman, G. C. Wang, M. Washington, T. M. Lu, *ACS Appl. Mater. Interfaces* **2020**, *12*, 35222; b) C. Chen, K. Li, F. Li, B. Wu, P. Jiang, H. Wu, S. Lu, G. Tu, Z. Liu, J. Tang, *ACS Photonics* **2020**, *7*, 352; c) M. R. Hasan, E. S. Arinze, A. K. Singh, V. P. Oleshko,

S. Guo, A. Rani, Y. Cheng, I. Kalish, M. E. Zaghloul, M. V. Rao, N. V. Nguyen, A. Motayed, A. V. Davydov, S. M. Thon, R. Debnath, *Adv. Electron. Mater.* **2016**, *2*, 1600182; d) G. Chen, W. Wang, C. Wang, T. Ding, Q. Yang, *Adv. Sci.* **2015**, *2*, 1500109.

[6] a) S. Agarwal, V. Nandal, H. Yadav, K. Kumar, *J. Appl. Phys.* **2021**, *129*, 203101; b) R. E. Williams, Q. M. Ramasse, K. P. McKenna, L. J. Phillips, P. J. Yates, O. S. Hutter, K. Durose, J. D. Major, B. G. Mendis, *ACS Appl. Mater. Interfaces* **2020**, *12*, 21730; c) J. Varghese, S. Barth, L. Keeney, R. W. Whatmore, J. D. Holmes, *Nano Lett.* **2012**, *12*, 868.

[7] a) T. D. C. Hobson, L. J. Phillips, O. S. Hutter, H. Shiel, J. E. N. Swallow, C. N. Savory, P. K. Nayak, S. Mariotti, B. Das, L. Bowen, L. A. H. Jones, T. J. Featherstone, M. J. Smiles, M. A. Farnworth, G. Zoppi, P. K. Thakur, T.-L. Lee, H. J. Snaith, C. Leighton, D. O. Scanlon, V. R. Dhanak, K. Durose, T. D. Veal, J. D. Major, *Chem. Mater.* **2020**, *32*, 2621; b) Y. B. Kim, J. S. Kim, S. K. Baek, Y. D. Yun, S. W. Cho, S. H. Jung, H. K. Cho, *Energy Environ. Sci.* **2018**, *11*, 2540.

[8] C. Chen, W. Li, Y. Zhou, C. Chen, M. Luo, X. Liu, K. Zeng, B. Yang, C. Zhang, J. Han, J. Tang, *Appl. Phys. Lett.* **2015**, *107*, 043905.

[9] M. Luo, M. Leng, X. Liu, J. Chen, C. Chen, S. Qin, J. Tang, *Appl. Phys. Lett.* **2014**, *104*, 173904.

[10] N. W. Tideswell, F. H. Kruse, J. D. McCullough, *Acta Crystallogr.* **1957**, *10*, 99.

[11] a) H. Song, T. Li, J. Zhang, Y. Zhou, J. Luo, C. Chen, B. Yang, C. Ge, Y. Wu, J. Tang, *Adv. Mater.* **2017**, *29*, 1700441; b) C. Chen, D. C. Bobela, Y. Yang, S. Lu, K. Zeng, C. Ge, B. Yang, L. Gao, Y. Zhao, M. C. Beard, J. Tang, *Front Optoelectron* **2017**, *10*, 18.

[12] a) C. Chen, J. Tang, *ACS Energy Lett.* **2020**, *5*, 2294; b) P. Fan, G. J. Chen, S. Chen, Z. H. Zheng, M. Azam, N. Ahmad, Z. H. Su, G. X. Liang, X. H. Zhang, Z. G. Chen, *ACS Appl. Mater. Interfaces* **2021**, *13*, 46671; c) G. Liang, M. Chen, M. Ishaq, X. Li, R. Tang, Z. Zheng, Z. Su, P. Fan, X. Zhang, S. Chen, *Adv. Sci.* **2022**, *9*, 2105142; d) T. Liu, X. Liang, Y. Liu, X. Li, S. Wang, Y. Mai, Z. Li, *Adv. Sci.* **2021**, *8*, 2100868; e) S.-N. Park, S.-Y. Kim, S.-J. Lee, S.-J. Sung, K.-J. Yang, J.-K. Kang, D.-H. Kim, *J. Mater. Chem. A* **2019**, *7*, 25900.

[13] a) H. Lei, J. Chen, Z. Tan, G. Fang, *Sol. RRL* **2019**, *3*, 1900026; b) Y. Zhou, L. Wang, S. Chen, S. Qin, X. Liu, J. Chen, D.-J. Xue, M. Luo, Y. Cao, Y. Cheng, E. H. Sargent, J. Tang, *Nat. Photonics* **2015**, *9*, 409; c) J. Dong, Y. Liu, Z. Wang, Y. Zhang, *Nano Sel.* **2021**, *2*, 1818; d) J. O. Mendes, E. D. Gaspera, J. van Embden, *Sol. RRL* **2022**, *6*, 2200265.

[14] C. Chen, K. Li, J. Tang, *Sol. RRL* **2022**, *6*, 2200094.

[15] a) Z. Li, X. Liang, G. Li, H. Liu, H. Zhang, J. Guo, J. Chen, K. Shen, X. San, W. Yu, R. E. I. Schropp, Y. Mai, *Nat. Commun.* **2019**, *10*, 125; b) Z. Duan, X. Liang, Y. Feng, H. Ma, B. Liang, Y. Wang, S. Luo, S. Wang, R. E. I. Schropp, Y. Mai, Z. Li, *Adv. Mater.* **2022**, *34*, 2202969; c) R. Tang, S. Chen, Z.-H. Zheng, Z.-H. Su, J.-T. Luo, P. Fan, X.-H. Zhang, J. Tang, G.-X. Liang, *Adv. Mater.* **2022**, *34*, 2109078.

[16] a) C. Liu, T. Liu, Y. Li, Z. Zhao, D. Zhou, W. Li, Y. Zhao, H. Yang, L. Sun, F. Li, Z. Li, *J. Mater. Chem. A* **2020**, *8*, 23385; b) S. Chen, T. Liu, M. Chen, M. Ishaq, R. Tang, Z. Zheng, Z. Su, X. Li, X. Qiao, P. Fan, G. Liang, *Nano Energy* **2022**, *99*, 107417.

[17] a) Y. Cao, P. Qu, C. Wang, J. Zhou, M. Li, X. Yu, X. Yu, J. Pang, W. Zhou, H. Liu, G. Cuniberti, *Adv. Opt. Mater.* **2022**, *10*, 2200816; b) S. Chen, Y. Fu, M. Ishaq, C. Li, D. Ren, Z. Su, X. Qiao, P. Fan, G. Liang, J. Tang, *InfoMat* **2023**, *5*, 12400.

[18] W. Li, L. Deng, X. Wang, J. Cao, Y. Xie, Q. Zhang, H. Zhang, H. Deng, S. Cheng, *Nanoscale* **2021**, *13*, 9834.

[19] R. Kondrotas, J. Zhang, C. Wang, J. Tang, *Sol. Energy Mater. Sol. Cells* **2019**, *199*, 16.

[20] L. Wang, D.-B. Li, K. Li, C. Chen, H.-X. Deng, L. Gao, Y. Zhao, F. Jiang, L. Li, F. Huang, Y. He, H. Song, G. Niu, J. Tang, *Nat. Energy* **2017**, *2*, 17046.

[21] K. Li, C. Chen, S. Lu, C. Wang, S. Wang, Y. Lu, J. Tang, *Adv. Mater.* **2019**, *31*, 1903914.

[22] X. Liang, Z. Li, X. San, T. Liu, Y. Liu, K. Shen, S. Wang, R. E. I. Schropp, Y. Mai, *Sol. RRL* **2021**, *6*, 2100869.

[23] a) S.-N. Park, S.-Y. Kim, S.-J. Lee, S.-J. Sung, K.-J. Yang, J.-K. Kang, D.-H. Kim, *Mater. Adv.* **2022**, *3*, 978; b) J. Zhou, H. Chen, X. Zhang, K. Chi, Y. Cai, Y. Cao, J. Pang, *J. Alloys Compd.* **2021**, *862*, 158703; c) F. Pattini, S. Rampino, F. Mezzadri, D. Calestani, G. Spaggiari, M. Sidoli, D. Delmonte, A. Sala, E. Gilioli, M. Mazzer, *Sol. Energy Mater. Sol. Cells* **2020**, *218*, 110724; d) Y. Pan, X. Hu, Y. Guo, X. Pan, F. Zhao, G. Weng, J. Tao, C. Zhao, J. Jiang, S. Chen, P. Yang, J. Chu, *Adv. Funct. Mater.* **2021**, *31*, 2101476; e) X. Liang, C. Guo, T. Liu, Y. Liu, L. Yang, D. Song, K. Shen, R. E. I. Schropp, Z. Li, Y. Mai, *Sol. RRL* **2020**, *4*, 2000294; f) S. Yao, J. Wang, J. Cheng, L. Fu, F. Xie, Y. Zhang, L. Li, *ACS Appl. Mater. Interfaces* **2020**, *12*, 24112; g) W. Wang, Z. Cao, L. Wu, F. Liu, J. Ao, Y. Zhang, *ACS Appl. Energy Mater.* **2021**, *4*, 13335; h) X. Wen, C. Chen, S. Lu, K. Li, R. Kondrotas, Y. Zhao, W. Chen, L. Gao, C. Wang, J. Zhang, G. Niu, J. Tang, *Nat. Commun.* **2018**, *9*, 2179; i) H. Deng, Y. Zeng, M. Ishaq, S. Yuan, H. Zhang, X. Yang, M. Hou, U. Farooq, J. Huang, K. Sun, R. Webster, H. Wu, Z. Chen, F. Yi, H. Song, X. Hao, J. Tang, *Adv. Funct. Mater.* **2019**, *29*, 1901720; j) B. Zhou, T. Kimura, Y. Okazaki, K. Hachiya, T. Sagawa, *ACS Appl. Nano Mater.* **2022**, *5*, 16082.

[24] T. D. C. Hobson, K. Durose, *Mater. Sci. Semicond. Process.* **2021**, *127*, 105691.

[25] H. Zhou, M. Feng, P. Li, X. Gong, D. Zhang, S. Chen, *Sustainable Energy Fuels* **2020**, *4*, 3943.

[26] Mamta, Y. S., K. K. Maurya, V. N. Singh, *Sol. Energy Mater. Sol. Cells* **2021**, *230*, 111223.

[27] A. Vanderdrift, *Philips Res. Rep.* **1967**, *22*, 267.

[28] H. Zhou, M. Feng, K. Song, B. Liao, Y. Wang, R. Liu, X. Gong, D. Zhang, L. Cao, S. Chen, *Nanoscale* **2019**, *11*, 22871.

[29] D. L. Smith, *Thin-Film Deposition: Principles and Practice*, McGraw-Hill Education, New York **1995**.

[30] S. Zhang, H. Wang, M. M. Kirchner, J. Liu, H. Luo, Y. Ren, C. Yuan, H. T. Hattori, A. E. Miroshnichenko, W. Lei, *Adv. Mater. Interfaces* **2022**, *9*, 2200448.

[31] J. A. Dean, N. A. Lange, *Lange's Handbook of Chemistry*, McGraw-Hill, New York **1992**.

[32] E. D. Gaspera, D. F. Kennedy, J. van Embden, A. S. R. Chesman, T. R. Gengenbach, K. Weber, J. J. Jasieniak, *Adv. Funct. Mater.* **2015**, *25*, 7263.

[33] Y. Tak, S. J. Hong, J. S. Lee, K. Yong, *J. Mater. Chem.* **2009**, *19*, 5945.